Enhancing Fatigue Life of Additive Manufactured Parts with Electrospark Deposition Post-processing

Pablo D. Enrique *[a], Ali Keshavarzkermani [a], Reza Esmaeilizadeh [a], Stephen Peterkin [b], Hamid Jahed [a], Ehsan Toyserkani [a], Norman Y. Zhou [a]

*Corresponding author: pdenriqu@uwaterloo.ca, 519-888-4567 ext. 35625
[a] University of Waterloo, 200 University Ave W, Waterloo, Ontario, N2L 3G1, Canada.
[b] Huys Industries Ltd., 175 Toryork Drive, Unit 35 Weston, Ontario, M9L 1X9, Canada

Abstract

Metal additive manufacturing processes allow for the production of highly dense parts with increased geometric freedom and less waste than traditional manufacturing techniques. However, one of the biggest challenges in using these parts is the relatively high surface roughness inherent to the manufacturing process. This roughness negatively affects fatigue properties and necessitates the use of post-processing surface treatments. Several methods are presented for improving local surface properties of laser powder bed fusion parts using electrospark deposition (ESD), hammer peening and heat-treatment processes. An optimized surface roughness reduction of 82 % and near-surface hardness increase of 85 % is obtained. Post-processed Hastelloy X parts reach $> 10^7$ cycles during fatigue testing at 350 MPa, in comparison to failure at 10^5 cycles in the as-built condition. The improvement in mechanical properties obtained with a combined ESD and peening process shows potential for the selective enhancement of critical surface regions in additive manufactured parts.

Keywords: Laser powder-bed fusion, Surface roughness, Fatigue, Electrospark deposition, Hastelloy X

1   **1.0 Introduction**

2   Additive manufacturing (AM) processes such as laser powder bed fusion (LPBF) provide significant advantages over
3   traditional manufacturing. With reduced material waste when compared to subtractive processes and considerable
4   geometrical freedom, LPBF is an especially attractive option for the manufacturing and lightweighting of parts made
5   from high value materials. However, despite significant research into the subject, LPBF parts still suffer from
6   relatively low surface quality. This has been shown to result in reduced fatigue performance, since fatigue cracks
7   frequently initiate from surfaces at locations with higher stress concentrations [1–3]. Increased surface roughness
8   can also negatively affect aerodynamic performance – such as in the case of turbine blades or vanes – by interacting
9   with the boundary layer of air that flows across the surface and introducing flow instabilities [4–6].

10 The causes of surface roughness have been attributed to a variety of factors, including print positioning on the build
11 plate [7], the ejection of spatter particles [8,9], the stair-step effect, and LPBF process parameters such as the printed
12 surface orientation and thermal history [7,10,11], linear energy density, laser power and hatch spacing [12,13].
13 Although process parameters can be optimized to obtain acceptable quality surfaces [14], the other contributing
14 factors make surface quality highly variable within a single part or between parts on the same build plate. For
15 commercial applications, some amount of post-processing that addresses surface quality is usually required.

16 Many surface finishing techniques are available and can be chosen based on the required final surface roughness,
17 desired surface properties, and geometrical complexity of the part being processed. Machining is a traditional
18 method for reducing external surface roughness [15,16], but results in material waste and is difficult to use on
19 complex geometries. Machining is also more challenging on work hardening materials such as Ni-superalloys [17]. A
20 reduction in surface roughness is possible via in situ layer re-melting [18] or post-process laser polishing [19] in
21 additive manufactured parts. This technique has been demonstrated for nonplanar surfaces as well [20], although
22 more geometrically complex parts with overhangs, lattice structures or internal channels that are not easily
23 accessible must be addressed using other techniques.

24 One technique for reducing the surface roughness of internal channels – abrasive flow machining – requires a fluid
25 with abrasive particles capable of eroding or producing micro-cuts on the part surface. Applications to additive
26 manufactured parts have found notable reductions in surface roughness [21], although the long processing times
27 and inconsistent material removal that depend on local shear strain rates introduce some challenges [22]. Another
28 technique is chemical etching or electropolishing, which is shown to achieve a significant surface roughness
29 reduction [23]. However, several disadvantages exist: this process often results in excessive material removal that
30 can affect part tolerances [24], large features are not easily removed, the preferential dissolution of some phases in
31 multiphase alloys can cause short range roughening [25], and conventional electropolishing methods are generally
32 expensive, hazardous to workers, and environmentally harmful [26]. A combination of surface finishing techniques
33 can be beneficial for applications that require a greater reduction in surface roughness and can overcome the
34 individual disadvantages of a single process [27]. A 2-step abrasive flow machining and electrochemical machining
35 process was successfully shown to reduce surface roughness by 80% in LPBF-made laser cutting nozzles, while
36 improving performance over the as-built condition to match that of a conventionally manufactured part [28].
37 Another example identifies a 3-step process of glass blasting, vibration deburring, and dry electropolishing capable
38 of reducing surface roughness by 93% [18].

39 The influence of surface finishing techniques on fatigue properties have been frequently demonstrated in literature.
40 Chemical etching of a LPBF part resulted in a 2 times improvement in fatigue life over the as-built condition [29].
41 Abrasive and impact surface finishing techniques have shown similar improvements in fatigue life; the use of
42 ultrasonic shot peening on thin struts built by electron beam melting was shown to achieve a 2 times improvement
43 in the cycles to failure, while sandblasting was shown to improve the cycles to failure by an order of magnitude [30].
44 The improvements are typically attributed to a reduced surface roughness, the introduction of compressive residual
45 stresses or microstructural changes.

46 Many of these surface finishing techniques have the common characteristic of deforming or removing material from
47 the surface. Rather than use a subtractive process, this study demonstrates the use of an additive electrospark
48 deposition (ESD) technique and machine hammer peening to reduce surface roughness while improving the
49 properties of external surfaces in LPBF-made Hastelloy X parts. The ESD process melts rough features on the part
50 surface and introduces beneficial surface properties by depositing an Inconel 718 coating, while machine hammer
51 peening flattens surface features and allows for longer ESD processing times. The combination of these two
52 processes achieves greater surface roughness reduction with shorter processing times than the individual
53 application of ESD or hammer peening. Several heat treatments are also investigated to address residual stresses

54 and promote a precipitation hardening effect in the deposited Inconel 718. Although Inconel 718 and Hastelloy X
55 are both Ni-superalloys, appropriate processing of Inconel 718 can obtain a significantly higher hardness and
56 strength than Hastelloy X [31]. As a result of ESD and hammer peening, the surface and fatigue properties of LPBF-
57 made Hastelloy X parts are significantly improved.

58 **2.0 Material and methods**

59 *2.1 Laser Powder Bed Fusion (LPBF)*

60 In this study, an EOS M290 equipped with an Ytterbium fiber laser and gas atomized Hastelloy X powder with a D50
61 (median diameter) of 29.3 μm were used to manufacture cubic LPBF parts (10 × 15 × 30 mm). All samples were made
62 with similar processing parameters (laser power of 200 W, laser velocity of 900 mm/s, layer thickness of 0.06 mm
63 and hatching spacing of 0.08 mm) using a rotated stripe scanning strategy. The build plate temperature was
64 maintained at 80 °C during the process. These samples were then post-processed for surface roughness analysis,
65 microhardness measurements, and microstructure characterization. The same process parameters were also used
66 to create fatigue testing samples described in section 2.4.

67 *2.2 Electrospark Deposition (ESD) and hammer peening*

68 The side surfaces of LPBF parts were post-processed using a manually operated ESD machine and handheld machine
69 hammer peening tool provided by Huys Industries. ESD operates by discharging a capacitor through a consumable
70 electrode and conductive substrate. A 3.2 mm diameter Inconel 718 electrode was used as shown in Figure 1a.
71 During the process, small molten droplets from the electrode (Figure 1b) are transferred to the substrate and
72 solidified (Figure 1c). Ultra-high purity argon shielding gas was delivered coaxially around the electrode during
73 deposition, and ESD parameters of 100 V, 80 μF and 150 Hz were used based on previous studies that show high
74 density and good mechanical properties [32,33]. Coatings were applied to 10 mm by 10 mm regions for various spark
75 durations (25 s, 75 s, 125 s) in a raster scan pattern, with the pattern rotated 90 ° between layers. The machine
76 hammer peening tool operates by driving a 2.5 cm long, 4.8 mm diameter hardened tool steel rod using a rotating
77 21 g weight offset by 0.64 mm (Figure 2). Rotation occurs at a frequency of 100 Hz, and the vibration amplitude at
78 the rod tip is 0.5 mm. When peening was used, the ESD process was stopped every 12.5 s and peening was applied
79 to the entire coated area.
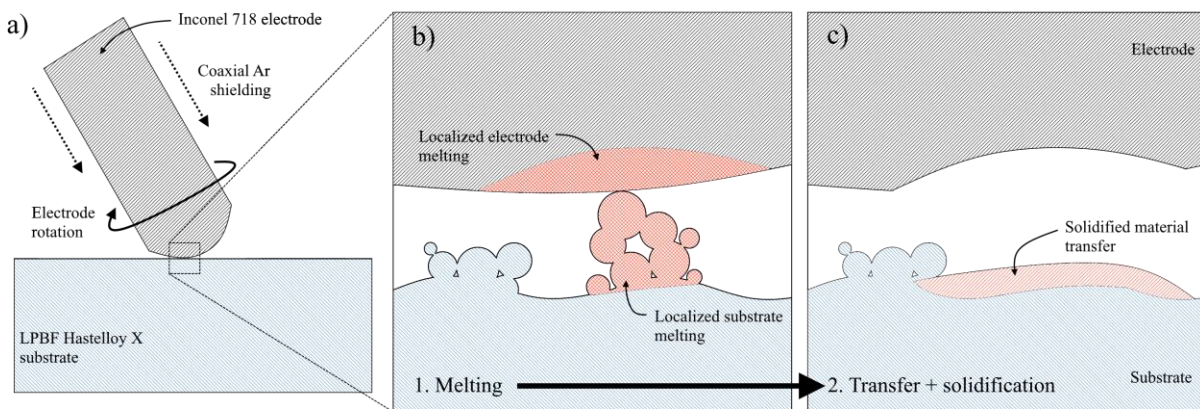
80
81 Figure 1. Simplified schematic of the ESD process showing a) overview of electrode and substrate, b) localized
82 melting of electrode and substrate during ESD, and c) material transfer and solidification

3
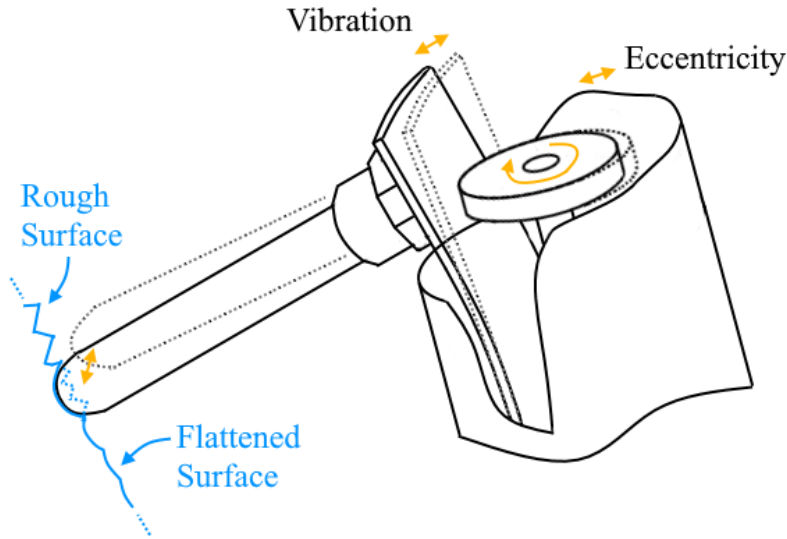
Figure 2. Schematic of hammer peening tool mechanism showing vibration of a rod driven by the rotation of an eccentric weight

2.3 Heat Treatment

Inconel 718 coated Hastelloy X samples were studied in several heat-treated conditions, described in Table 1. All heat treatments were performed in a horizontal quartz tube furnace under ultra-high purity argon gas, with a flow rate of 4 L/min and 250 Pa of positive pressure. The aging temperature and time is selected based on the industry standard for Inconel 718 [34], and the solution annealing temperature and time is selected based on literature studies of secondary phase dissolution in rapid solidification processed Inconel 718 [35].

Table 1. Heat treatments for Inconel 718 coated Hastelloy X samples

Sample	Heat Treatment
Direct Aged (DA)	720 °C for 8 hrs, 620 °C for 10 hrs, air cooled
Solution Annealed (SA)	1100 °C for 1 hr, water quenched
Solution Annealed and Aged (SAA)	1100 °C for 1 hr, water quenched 720 °C for 8 hrs, 620 °C for 10 hrs, air cooled

2.4 Characterization

Microstructure characterization was performed using a Zeiss UltraPlus scanning electron microscope (SEM) with an AMETEK EDAX Apollo XL energy-dispersive X-ray spectroscopy (EDX) attachment. A TESCAN SEM was used for the analysis of fatigue fracture surfaces, and an Oxford electron backscatter diffraction (EBSD) detector in a JEOL7000F SEM was used for analysis of samples after heat treatment. A surface profile was obtained with a Keyence VK-X250 confocal laser microscope, and hardness results were obtained using a load of 0.1 kgf on a Wolpert Wilson 402 MVD micro Vickers hardness tester.

A combination of ESD, peening and heat treatments were used to create several post-processed samples for surface profile analysis, microhardness evaluation and fatigue testing. A breakdown of samples created for each analysis is provided in Table 2.

Table 2. Post-processed LPBF Hastelloy X samples

Analysis	Sample	Sample Description
Surface Profile	As-built	No surface treatment
	ESD	With ESD Inconel 718 coating
	ESD+HP	With ESD Inconel 718 coating and hammer peening
	HP	With hammer peening
Microhardness	ESD	With ESD Inconel 718 coating
	ESD+HP	With ESD Inconel 718 coating and hammer peening
	ESD+HP+DA	With ESD Inconel 718 coating, hammer peening and direct aging heat treatment
	ESD+HP+SA	With ESD Inconel 718 coating, hammer peening and solution annealing heat treatment
	ESD+HP+SAA	With ESD Inconel 718 coating, hammer peening, and solution annealing + aging heat treatment
Fatigue life	As-built	No surface treatment
	HP	With hammer peening
	ESD+HP	With ESD Inconel 718 coating and hammer peening
	ESD+HP+DA	With ESD Inconel 718 coating, hammer peening and direct aging heat treatment

105

106 *2.5 Fatigue testing*

107 Post-processing of ESD+HP samples for fatigue testing consists of two layers of ESD Inconel 718 applied to the necked
108 region of the fatigue specimens (built in a vertical orientation with dimensions shown in Figure 3a), with peening
109 performed at the conclusion of each layer. A second set of post-processed HP samples received an equivalent
110 amount of peening as ESD+HP samples, without the application of an Inconel 718 coating using ESD. The last set of
111 post-processed samples (ESD+HP+DA) were processed similarly to the ESD+HP samples, with the addition of a direct
112 aging heat treatment. The resulting post-processed samples are compared to samples in the as-built condition,
113 shown in Figure 3b.

114 An Instron 8872 servohydraulic fatigue testing system was used to test the room temperature fatigue performance
115 of LPBF Hastelloy X samples with and without post-processing using a stress ratio (R = $\frac{S_{min}}{S_{max}}$) of 0.1 in tension-tension
116 mode. Low cycle fatigue testing was performed at a maximum stress of 550 MPa while the high cycle fatigue testing
117 was done at a maximum of 350 MPa. A frequency of 5 Hz was used for all samples except the post-processed samples
118 tested at high cycle fatigue conditions. These samples were tested at a frequency of 5 Hz until 10^6 cycles, and then
119 switched to 30 Hz due to the long test durations.
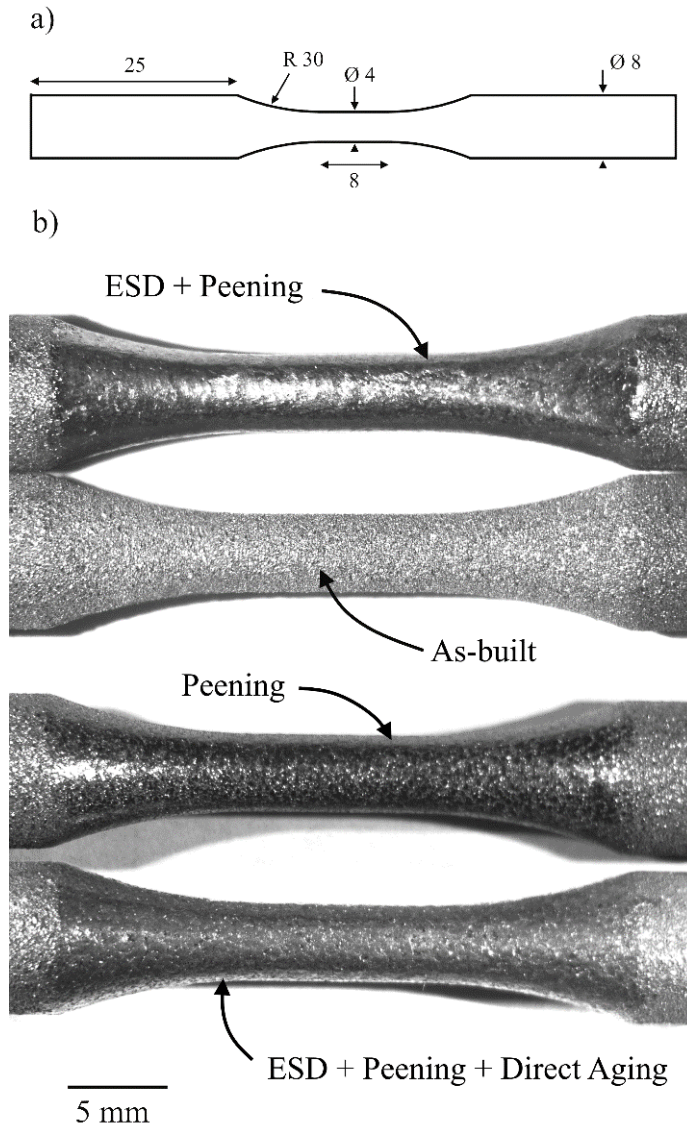
Figure 3. a) Fatigue testing specimen dimensions in mm and b) samples in the as-built and post-processed conditions

2.5 Surface profile processing

To distinguish long-range and short-range imperfections (waviness and roughness), raw height data (Figure 4a) was processed in MATLAB by applying a gaussian filter according to ISO 16610-21 [36]. The long wave component (Figure 4b) was used to calculate the arithmetic mean height of the surface waviness (W_a), while the short wave component (Figure 4c) was used to calculate the arithmetic mean height of the surface roughness (S_a).
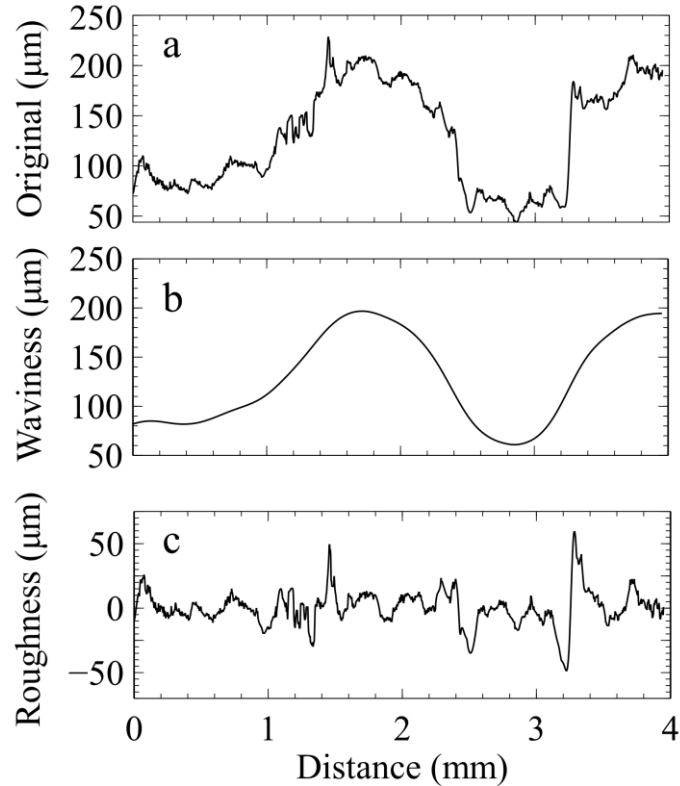
Figure 4. a) Original surface profile of an as-built sample, b) long wave portion of surface profile, and c) short wave portion of surface profile

3.0 Results and discussion

3.1 ESD post-processing

3.1.1 Surface roughness

The most notable features on the side surface of as-built parts are the partially fused particles (PFPs) shown in Figure 5a. The adherence of these powder particles to the side surface can be attributed to loose powder adjacent to the melt pool or spatter directed into the melt pool during the LPBF process [8]. In these conditions, partial melting of the powder in the liquid melt pool or the formation of sinter necks between the powder and the recently solidified melt pool will occur. Some roughness can also be attributed to the underlying surface, which shows distinct melt pool tracks because of the contour step performed on each layer. Since the side walls are vertical, other common contributors to surface roughness – such as the staircase effect in which angled surfaces are created using discrete steps – are not present [7].

After a short 25 s ESD time, the surface shows splash features (Figure 5b) as a result of material transfer from the electrode. PFPs are no longer visible, likely due to re-melting of the substrate surface and coverage by material transferred from the electrode during ESD. A notable improvement to surface roughness is obtained by intermittent peening during ESD, and is clearly visible in the ESD+HP sample shown in Figure 5c. Although deposition time is also 25 s, splash features are not visible, and the uneven surface has been mostly flattened except for some regions that were too deep to reach with the peening tool.

The etched cross-section of an ESD+HP sample part after 75 s of ESD processing time is shown in Figure 6a. A closer look at the interface between the coating and substrate shows evidence of the Hastelloy X surface melting during

7

150 ESD that removes PFPs from the surface. The cross-section in Figure 6b shows a Hastelloy X particle – distinguishable
151 due to its equiaxed grain structure – that has been partially melted by the ESD process. The composition profile
152 shown in Figure 6c identifies a 10 μm region of deposited material with lower Nb and greater Mo content than is
153 expected from Inconel 718. Due to the spot size limitations of EDX measurements, the transition region in which
154 Hastelloy X and Inconel 718 mix can be said to be 10 μm or less in size. Good metallurgical compatibility is expected
155 based on the similar compositions of both materials, and the SEM/EDX analysis was unable to identify any
156 intermetallics in the transition region.
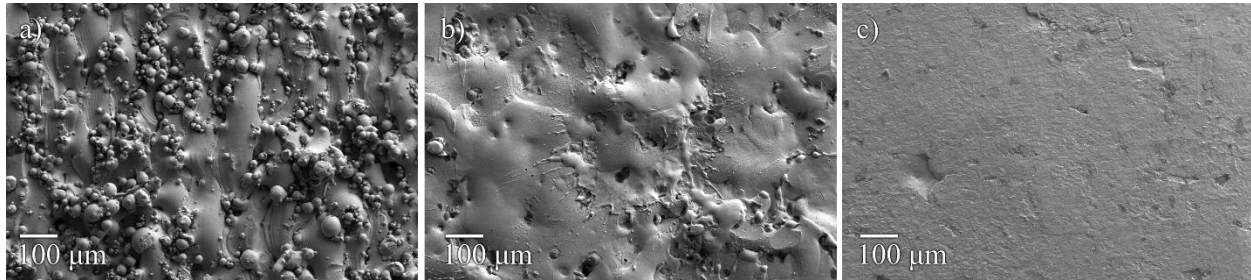
157

158 Figure 5. SEM images of the side surface of an as-built LPBF Hastelloy X part a) in the as-built condition, b) after
159 ESD coating of Inconel 718 without peening, and c) after ESD coating of Inconel 718 with peening (ESD+HP)
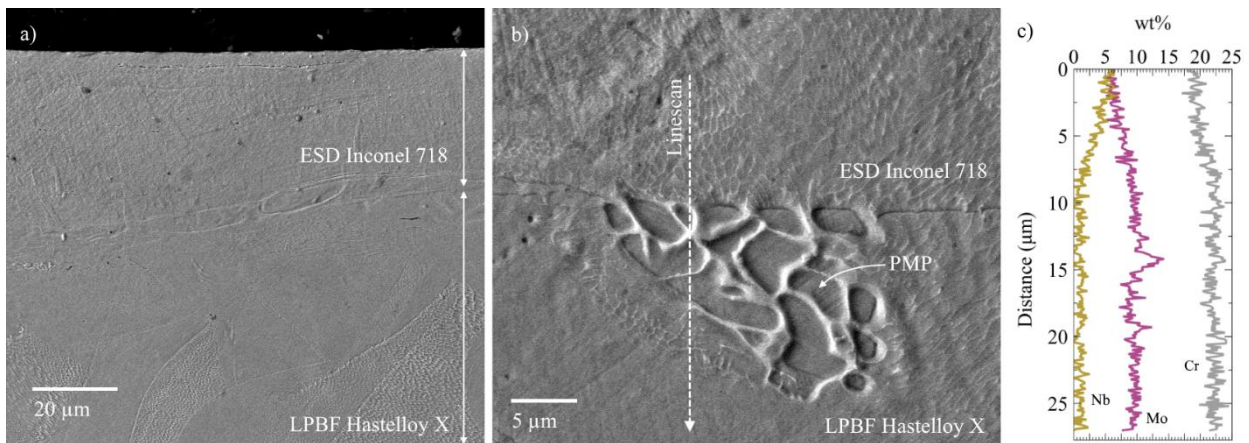
160

161 Figure 6. SEM images of a) an etched ESD+HP sample cross-section, b) partially melted particle visible at the
162 coating/substrate interface, and c) EDX line-scan as indicated in (b).

163 As shown in Figure 7a, the short deposition times (25 s) decrease the short-range surface roughness from an initial
164 S_a of 13.2 μm in the as-built samples to 6.7 μm in ESD processed samples, 6.5 μm in hammer peened (HP) samples,
165 and 2.4 μm in ESD+HP samples (49%, 51%, and 82% decreases, respectively). The waviness also decreases from the
166 as-built condition although to a lesser extent, from a W_a of 8.8 μm to 7.2 μm in ESD samples, 6.3 μm in hammer
167 peened (HP) samples and 4.9 μm in ESD+HP samples (18%, 28%, and 45% decreases, respectively). The surface
168 profiles shown in Figure 7c clearly show the effect of ESD on the surface roughness and waviness. The initial as-built
169 surface has small localized peaks attributed to PFPs that are the major contributor to surface roughness, which are
170 removed by the ESD process. Some longer-range waviness is present on the as-built surface and remains relatively
171 unchanged after 25s of ESD processing. With longer deposition times and increased material deposition these wavy
172 features grow preferentially while the roughness remains below the as-built condition.

173 The ability of peening to maintain a low surface waviness in conjunction with ESD can be attributed to the mechanism
174 by which ESD occurs. As described in [37], irregular contact geometry strongly influences where the current
175 discharge, spark discharge, and mass transfer occurs. Current discharge occurs when the electrode and substrate

176 make contact, which on a wavy substrate surface is at the highest protruding region. When the contact is broken,
177 spark discharge occurs, and molten droplets are transferred from the electrode to the substrate. Due to strong
178 electrostatic forces, material is preferentially transferred to high points on the substrate surface [37,38]. When using
179 ESD on a LPBF-made surface, current discharge initially occurs through clusters of protruding PFPs. The sinter necks
180 that join these PFPs to the bulk part provide for a poor connection, resulting in higher resistance to current discharge,
181 increased joule heating and lower thermal diffusion. The result is an initial melting of these features (Figure 5b),
182 which reduces the surface roughness even without the use of peening (seen in Figure 7a for short deposition times
183 of 25 s). Further depositions produce elevated regions that further exacerbate the uneven transfer of material,
184 forming islands as shown in Figure 7c. However, the use of intermittent peening during ESD slows the preferential
185 deposition on elevated regions by flattening surface irregularities that appear at shorter intervals (roughness) and
186 preventing preferential buildup on these irregularities from forming longer interval defects (waviness). This allows
187 longer deposition times to have more uniform coatings.

188 The surface melting caused by ESD is critical to achieving a low surface roughness at short processing times; a
189 comparison to samples which were only peened (HP) in Figure 7a shows that a combination of ESD and hammer
190 peening is required to obtain low surface roughness, with either process being less effective when used alone. In
191 conjunction with peening, an ESD process can be used to address both the need for reduced surface roughness and
192 to change the surface properties of LPBF parts.
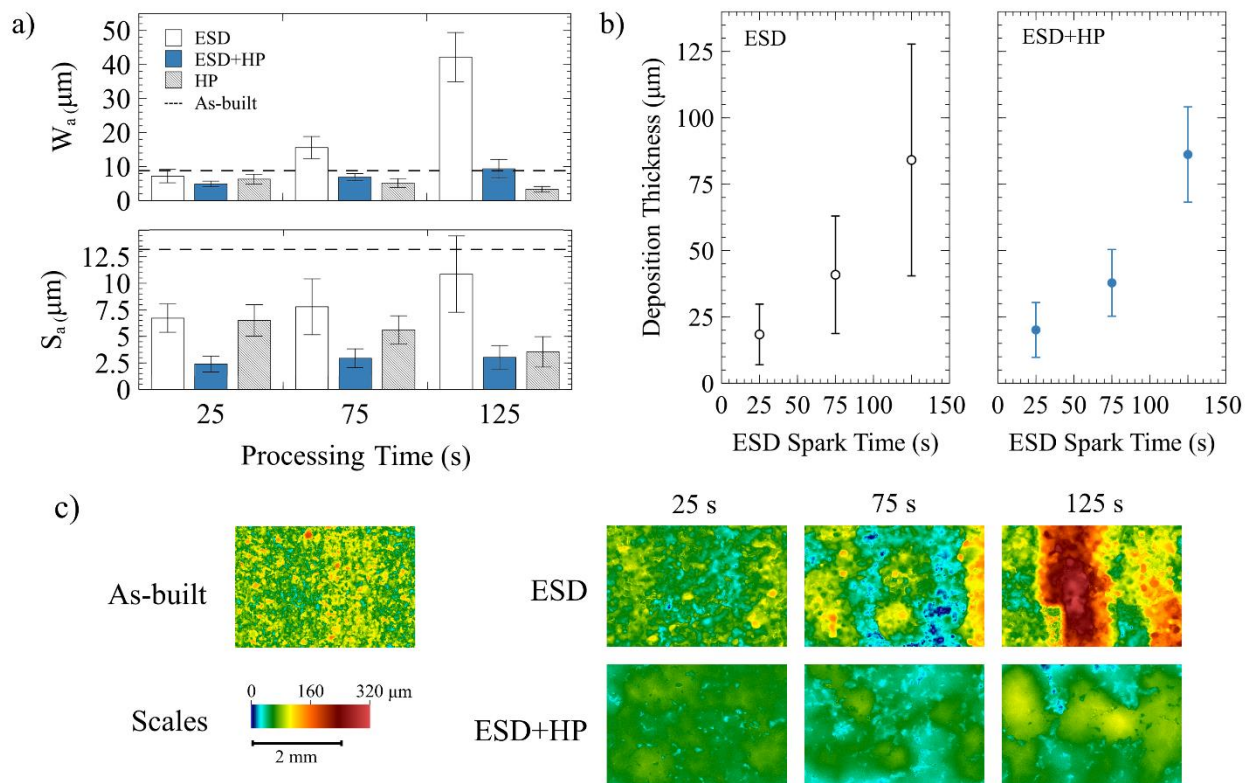
194 Figure 7. Comparison of a) surface roughness with standard deviations, b) coating thickness with standard
195 deviations, and c) 2D surface roughness maps for ESD coatings made using various deposition times for as-built,
196 ESD, and ESD+HP processed samples

197 The use of peening – and by extension the surface condition of the part being coated – in ESD+HP samples has no
198 effect on the deposition thickness (Figure 7b), although it does have an effect on the coating distribution by

199 minimizing the surface waviness as described previously. The similarities in deposition thickness can be seen in
200 Figure 7b, along with a clear difference in the standard deviation of peened (ESD+HP) and non-peened (ESD) samples.
201 This unequal variance is quantified with the use of a Levene test [39], which shows in Table 3 a significant difference
202 in the variance of the thicknesses between ESD+HP and ESD samples after 75s and 125s of ESD spark time. With the
203 use of a Box-Cox transformation (λ=0.3) to meet the assumptions of a normal distribution and equal variance
204 required for an ANOVA, the effect of peening, deposition time, and their interaction could be analyzed. Only
205 deposition time was found to influence the deposition thickness (Table 4), with p-values for peening or the
206 interaction between the two factors above 0.05. These results, which suggest that the use of peening has no effect
207 on the average deposition thickness but does reduce variance in the deposition thickness at longer deposition times,
208 indicates that the quantity of material transferred during ESD is not affected by the morphology of the substrate
209 surface. Instead, only the distribution of the transferred material changes when peening is used.

210   Table 3. Levene test for average deposition thickness data in Figure 7b comparing ESD+HP and ESD samples

|		ESD Spark Time		
Test	**Null Hypothesis (NH)**	**25s**	**75s**	**125s**
Levene	There is no difference in the variation of the deposition thickness	p = 0.568 Fail to reject NH	p < 0.001 Reject NH	p < 0.001 Reject NH

211

212   Table 4. Average deposition thickness ANOVA for the effect of peening and deposition time (Figure 7b)

|	Sum of Squares	df	Mean Square	F	p
Peening	3.44	1	3.44	1.52	0.218
Time	1671.4	2	835.7	369.78	< .001
Peening $\times$ Time	5.49	2	2.75	1.22	0.297
Residuals	1299.5	575	2.26		

213

3.1.2 Microstructure and hardness

215 Inconel 718 coatings in ESD+HP samples show significantly higher hardness than LPBF Hastelloy X (471 HV vs. 283
216 HV), as well as the formation of a roughly 200 μm wide thermo-mechanically affected zone (TMAZ) in the Hastelloy
217 X near the deposition interface (Figure 8a). The effect of peening on hardness in both the deposition and TMAZ is
218 made clear in Figure 8b, which shows a 47 HV decrease and significant reduction of the TMAZ when peening is not
219 used (ESD samples). However, the deposition hardness without peening (424 HV) is still high when compared to
220 Inconel 718 in the cast (225 HV), LPBF (325 HV) or electron beam melted (355 HV) condition [40]. The difference is
221 attributed to a faster cooling rate that forms a sub-micron cellular microstructure (Figure 9a) and the presence of
222 fine secondary phases (Figure 9b) that form during deposition [41,42]. Some secondary phases are identified using
223 EDX as oxides, ranging from sub-micron sizes to several tens of microns. As seen clearly in Figure 9c, the oxides are
224 rich in Al, Ti, and Nb, while also containing similar Cr and Mo content as the surrounding matrix. The following
225 elements are arranged in terms of high to low standard free energies of formation for their oxides: Al, Ti, Nb, Cr, Fe,
226 Mo, and Ni [43]. As such, the inclusion of Mo in the oxide is unusual and may be attributed to EDX peak overlap with
227 Nb. The formation of these oxides is a common issue even in well-controlled high purity argon atmospheres [44,45],
228 and may be assisted by the diffusion and segregation of elements at elevated temperatures that are favourable to
229 oxidation [46].
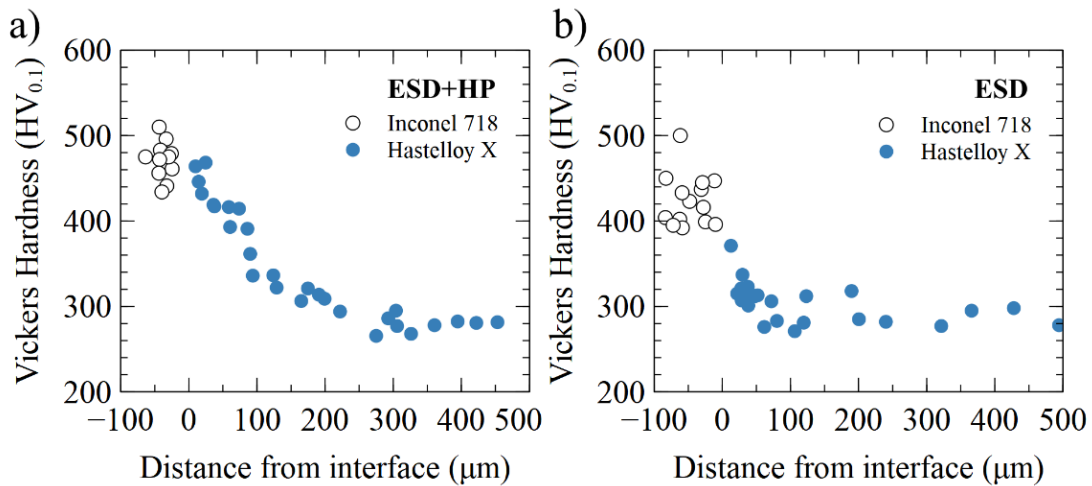
Figure 8. Microhardness values for Inconel 718 coating on Hastelloy X a) with peening (ESD+HP samples) and b) without peening (ESD samples)

The LPBF Hastelloy X substrate also exhibits a cellular subgrain microstructure (Figure 10a) with approximately twice the primary dendrite spacing compared to the ESD processed Inconel 718 (0.8 μm vs. 0.4 μm). Oxides were also identified within as-built LPBF Hastelloy X (Figure 10b), although with slight differences in composition compared to ESD processed Inconel 718. The oxides were determined to contain Al, Ti, and Cr, but no Mo or Nb were detected. The lack of Nb is expected since Hastelloy X does not contain Nb, while the lack of Mo can be explained by the lower oxidation potential of Mo compared to Al, Ti and Cr, as well as no opportunity for peak overlap with Nb.
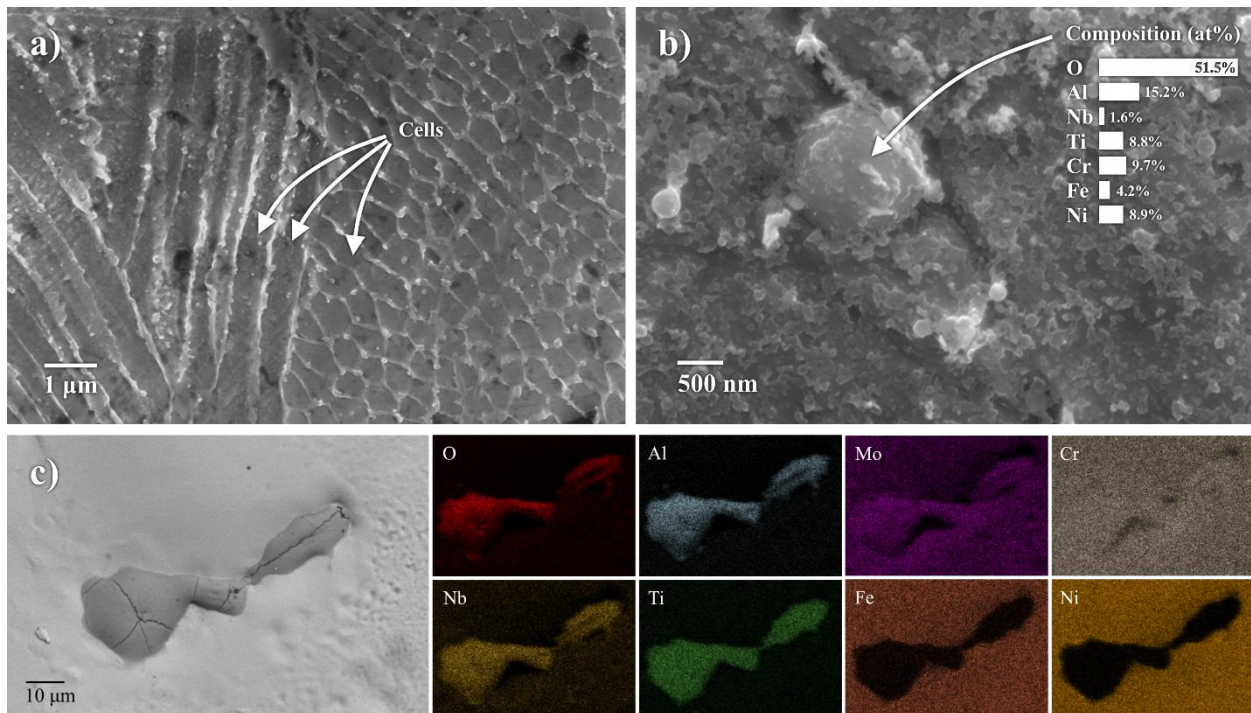
Figure 9. Microstructural features found within ESD Inconel 718 coating, including a) cellular dendritic subgrains, b) small spherical oxide with EDX composition, and c) large irregularly shaped oxide with corresponding EDX composition maps

11
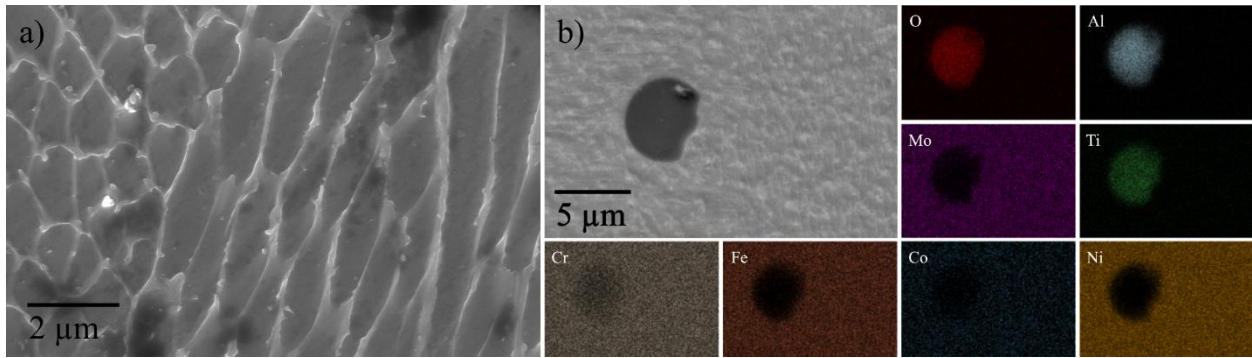
Figure 10. Microstructural features found within LPBF Hastelloy X, including a) cellular subgrains and b) irregularly shaped oxide with corresponding EDX composition maps

3.2 Heat treatment of ESD post-processed parts

Three heat treatments are investigated to determine their effect on microstructure and hardness of ESD+HP samples. The first is a direct aging heat treatment that aims to precipitate the strengthening γ" phase in the deposited Inconel 718 coating. The result of this treatment on microhardness is shown in Figure 11a. The second is an annealing heat treatment that aims to solutionize interdendritic phases, recrystalize the cellular microstructure, and remove residual stresses in the Inconel 718 coating. The result of this treatment on microhardness is shown in Figure 11b. The third heat treatment is a combination of the prior two; a solution annealing step is performed, followed by an aging heat treatment. The result is shown in Figure 11c.
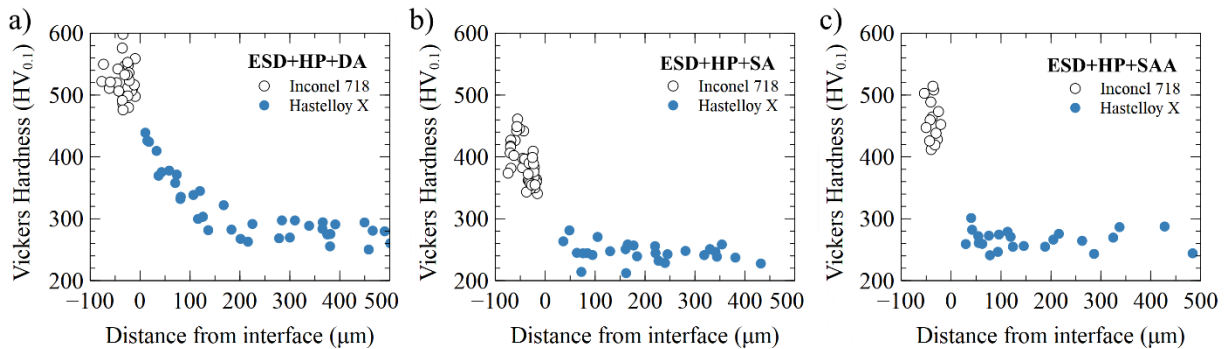
Figure 11. Microhardness values for peened Inconel 718 coating on Hastelloy X after a) direct aging (ESD+HP+DA samples), b) solution annealing (ESD+HP+SA), and c) solution annealing and aging (ESD+HP+SAA)

Similar to the previously reported effect of direct aging on ESD processed Inconel 718 [33], ESD+HP+DA samples show an increased Inconel 718 hardness of 523 HV (from 471 HV) while having no significant effect on the TMAZ or Hastelloy X substrate. Aging of Inconel 718 results in the formation of carbides (Figure 12a,b) and the formation of γ" and γ' precipitates (Figure 12c) with Ni_3Nb and $Ni_3(Al,Ti)$ compositions, respectively. Since these samples are direct aged without a solutionizing step, the interdendritic eutectic and potential Laves phase that forms during solidification is retained (Figure 12d). Without sufficient quantities of Nb, Al, or Ti in Hastelloy X, the typical γ" and γ' precipitates that contribute to an increase in strength and hardness after aging in other Ni-superalloys do not form. As such, only the deposited Inconel 718 is expected to noticeably benefit from the direct aging heat treatment.
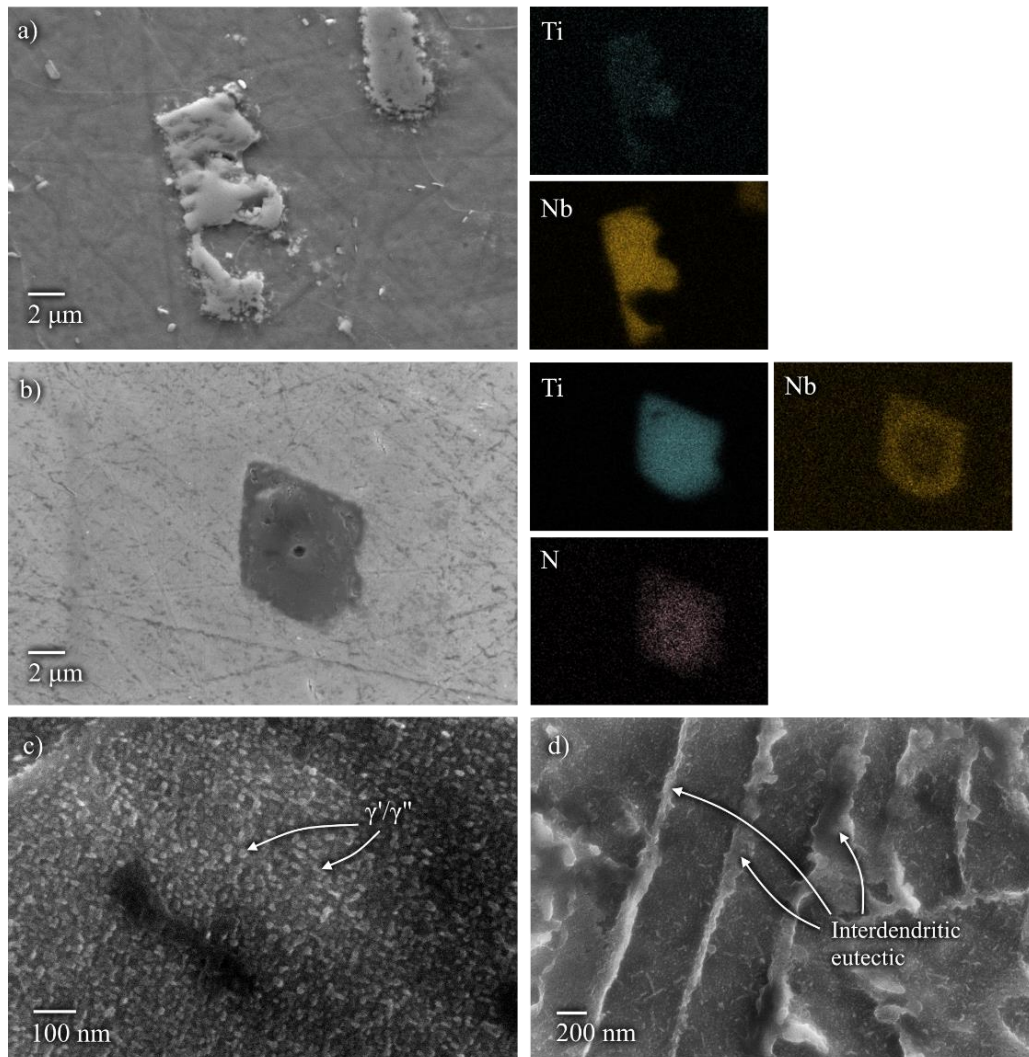
Figure 12. SEM images of phases obtained after aging Inconel 718, including a) (Nb,Ti)C, b) (Ti,Nb)CN, c) γ" and γ' and d) retained interdendritic eutectic after direct aging that formed during solidification

The use of a solution annealing heat treatment in ESD+HP+SA samples reduces hardness in the deposition (from 471 HV to 390 HV) and in the TMAZ (Figure 11b). This is attributed to the microstructural changes in the coating area after the solutionizing heat-treatment. To better characterize these changes, EBSD analysis has been performed. In the ESD+HP sample coatings, the inability to obtain clear EBSD results (Figure 13a) is due to severe distortion in the highly deformed coating region. Literature has shown that more advanced indexing techniques are required to resolve the low quality Kikuchi patterns obtained in this region [47]. The inability to index ESD coatings also occurred in ESD sample coatings without peening, and therefore cannot be attributed solely to stresses introduced by peening. Some residual stresses can be attributed to two additional mechanisms: quenching of transferred material upon contact with a substrate that constrains its thermal contraction, and differences in coefficients of thermal expansion leading to thermal stress [48]. The very rapid cooling experienced during ESD makes the first mechanism a likely source of residual stresses, while the similar material composition between the Inconel 718 coating and Hastelloy X substrate suggests a smaller contribution from differing coefficients of thermal expansion. The resulting distorted crystal structure causes Kikuchi bands to appear diffuse [49], making EBSD analysis of grain orientation difficult. Shrinkage also affects the substrate as seen in the Kernel average misorientation (KAM) maps, which show

13

that the local misorientation is increasing from the substrate core to the substrate/coating interface (Figure 13b). The higher misorientation near the interface is attributed to the combination of peening and ESD, during which the first mechanism – shrinkage of the coating during cooling – and peening both apply a compressive stresses on the substrate and distort the crystal structure of the grains. This results in more geometrically necessary dislocations, which corresponds to the higher hardness in the Hastelloy X substrate near the interface.

After solution annealing, the dislocation annihilation and rearrangement that occurs during recovery allows for proper indexing of the coating (Figure 13c). A narrow misoriented region with a columnar grain morphology (Figure 13d) is found in the coating surrounded by equiaxed ultrafine grains. This region of high misorientation is related to the pre-existing columnar grains which form due to epitaxial grain growth during rapid solidification. However, the misorientation-free regions in both the coating and TMAZ (Figure 13d) reveals that static recrystallization occurs, with much finer recrystallized grains in the coating than in the substrate. With high dislocation density being a driving force for recrystallization, the difference in final grain size can be attributed to the higher misorientation originally present in the coating that increases the nucleation rate during recrystallization. As such, even after an annealing heat treatment, the deposition hardness remains above that of cast, LPBF and EBM Inconel 718. In addition to the ultrafine grain size, some secondary phases such as oxides are not solutionized during the heat treatment and continue to contribute to the increased hardness.
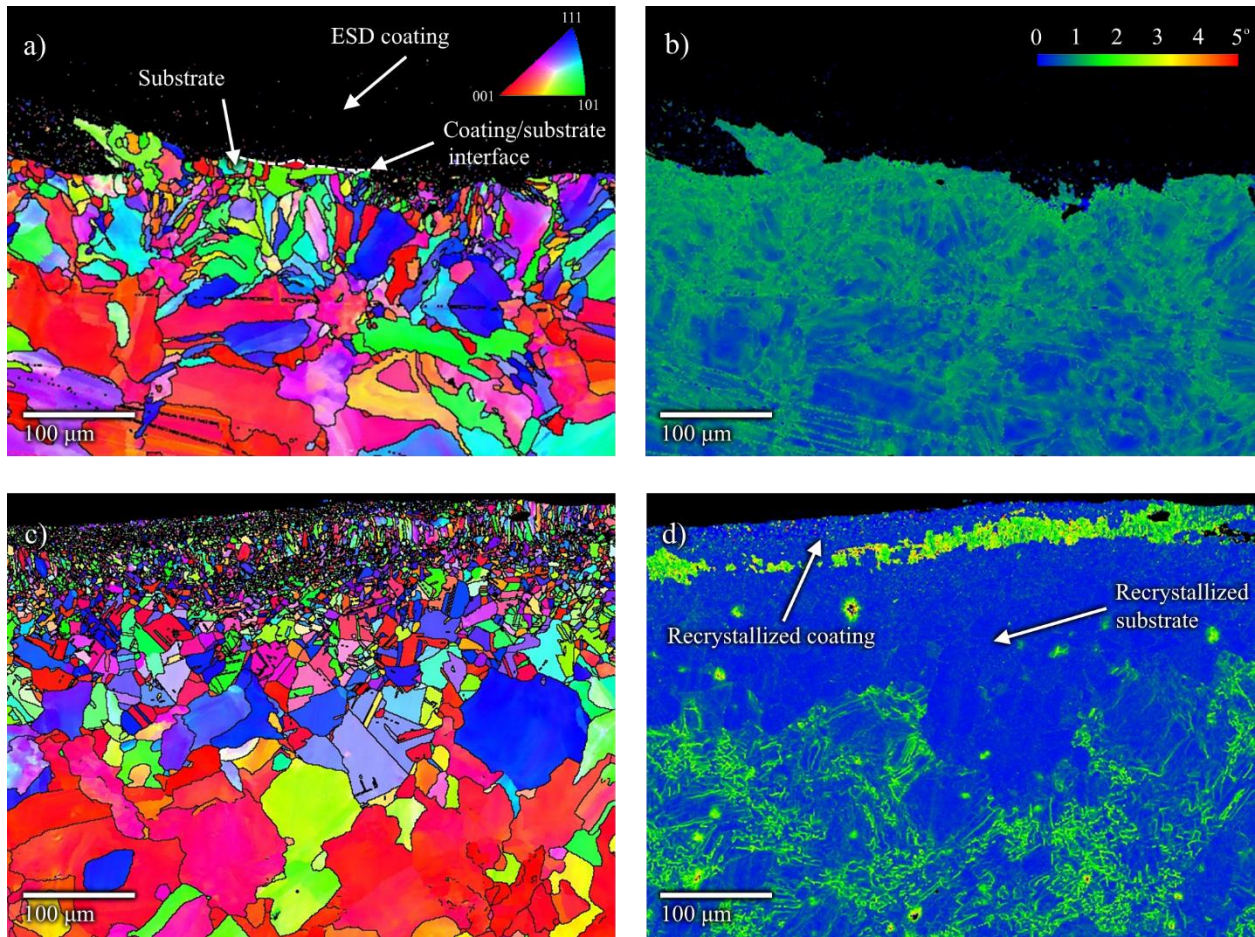

Figure 13. EBSD maps for a) as-deposited coating and substrate, b) KAM map of the as-deposited sample, c) annealed and aged (ESD+HP+SAA) sample, and d) KAM map of the annealed and aged (ESD+HP+SAA) sample

301 At the conclusion of an aging heat treatment performed on solution annealed samples (ESD+HP+SAA), the hardness
302 of the deposition increases to 460 HV. The 70 HV increase in the Inconel 718 hardness when comparing the annealed
303 coating to the annealed and aged condition is attributed to the precipitation of the γ" phase. However, since residual
304 stresses and some secondary phases have been removed during annealing, the deposition is 63 HV softer in the
305 annealed and aged state when compared to the direct aged state.

306 A comparison of time-temperature-transition diagrams show that Inconel 718 is more sensitive than Hastelloy X to
307 an aging heat treatment at 720 °C, with Inconel 718 forming the beneficial γ" phase [50]. This explains the
308 significantly greater effect of aging on the hardness and strength of Inconel 718. Due to the lack of precipitation
309 strengthening in Hastelloy X, the hardness outside of the TMAZ does not differ significantly after heat treatments.
310 However, the annealing treatment may alleviate some residual stresses that occur during LPBF, which may account
311 for the 38 HV drop between the as-built and annealed condition in Figure 11b. Both materials also form carbide
312 phases rapidly at 720 °C, with Hastelloy X forming M_6C and $M_{23}C_6$ carbides [51]. These often have a negative influence
313 on ductility in Hastelloy X, in addition to the negative influence on ductility from the sigma phase that forms between
314 650 °C and 760 °C [52].

3.3 Fatigue Response

316 The room temperature low and high cycle fatigue responses (LCF and HCF, respectively) of as-built LPBF Hastelloy X
317 are compared in Figure 14 to post-processed specimens in the hammer peened (HP), ESD and hammer peened
318 (ESD+HP), and ESD and hammer peened with a direct aging heat treatment (ESD+HP+DA) conditions. Two stress
319 levels, 550 MPa for LCF and 350 MPa for HCF, were chosen for comparison, and three samples per each condition
320 were tested at each stress level. The best performing condition (ESD+HP) showed a fatigue life improvement from 3
321 times to two orders of magnitude depending on the stress level. Most ESD+HP samples tested in LCF conditions
322 showed a fatigue life improvement of up to 5 times, whereas those tested in HCF conditions experienced runout (>
323 10^7 cycles) for a minimum fatigue life improvement of 50 times. However, one ESD+HP sample at each test condition
324 failed sooner, showing only 3- and 10-times improvement (for LCF and HCF, respectively) over the as-built condition.
325 Early fatigue failure is attributed to sub-surface lack of fusion defects, while failure of the better performing samples
326 occurred in the Inconel 718 coating due to surface defects during ESD. Further failure analysis is provided in Figure
327 15. Other post-processed conditions achieved smaller improvements in fatigue life over the as-built condition. The
328 use of hammer peening alone (HP samples) provided a 1.7- and 2.4-times improvement at LCF and HCF conditions,
329 respectively, while the ESD+HP+DA samples showed a 2- and 10-times improvement, respectively.
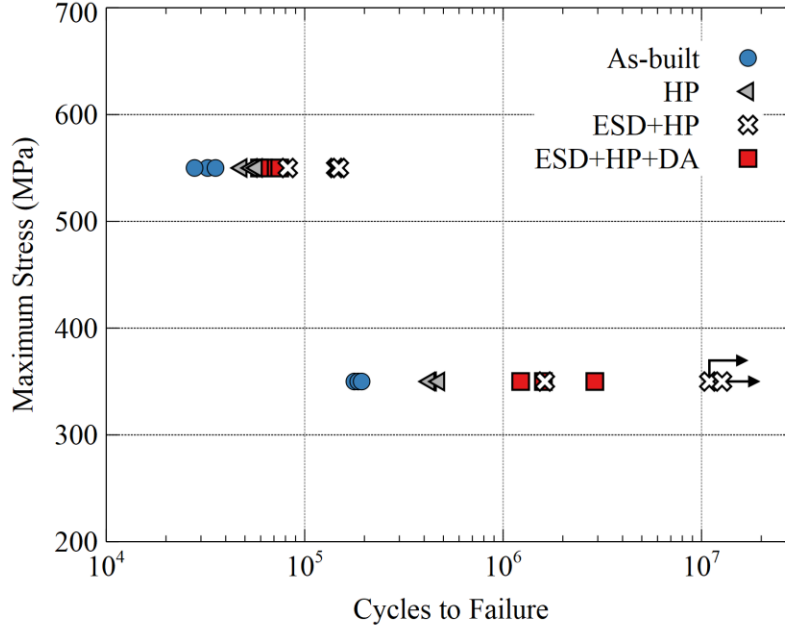
Figure 14. Results of fatigue testing as-built and post-processed specimens in LCF and HCF conditions. Arrows indicate samples with interrupted tests without failures up to 10^7 (runout).

Even with defects arising from LPBF and ESD, the fatigue life of samples in the ESD+HP condition are significantly improved. A comparison with the recent literature shows that the proposed ESD+HP post-processing is more effective in increasing the fatigue performance than a combined polishing (to S_a of 0.33 μm) and hot isostatic pressing (HIP) technique, which could only achieve up to 9×10^5 cycles at a maximum stress of 350 MPa [53]. The significant improvement obtained by ESD+HP over the as-built or polished and HIPed condition reported in the literature can be attributed to a combination of factors including the reduction in surface roughness, the higher strength of the as-built Hastelloy X substrate and Inconel 718 coating, and residual stresses introduced as a result of hammer peening and quenching stress during ESD.

ESD parameters for the ESD+HP samples were chosen specifically to reduce the as-built surface roughness of 13.2 μm to a post-processed S_a of 2.4 μm, in accordance with the results presented earlier (Figure 7a). This reduction in surface roughness has the effect of reducing the size of notch-like features at the surface, which often act as stress risers and crack initiation sites. The influence of roughness is reflected in calculations of the endurance limit stress ($\Delta\sigma_D$), which is effectively the maximum stress below which the crack propagation of a defect does not occur. Equation 1 is used while implementing a linear fracture mechanics approach [54]:

$$\Delta\sigma_D = \frac{\Delta K_{th}}{f K_t \sqrt{\pi a}} \qquad (1)$$

where f is a crack geometry dependent factor (1.122 for surface cracks), ΔK_{th} is the threshold stress intensity for crack propagation, a is the crack length and K_t is a stress concentration factor dependent on surface roughness. This dependence for a sample under a tensile stress state is shown in Equation 2 [55]:

$$K_t = 1 + 2\left(\frac{S_a}{\rho}\right)\left(\frac{S_y}{S_z}\right) \qquad (2)$$

where S_a is the arithmetic mean height, ρ is the valley profile radius, S_y is the maximum absolute peak to valley height, and S_z is the 10-point height. The description of K_t in Equation 2 incorporates several roughness and geometrical parameters that describe the influence of surface roughness on crack propagation from a surface notch, which is effective at predicting the fatigue life of additive manufactured parts [56]. Values of these roughness

16

354 parameters for an ESD post-processed surface and original as-built surface are shown in Table 5. The use of these
355 parameters in Equation 2 suggests a decrease in the stress concentration factor (K_t) after ESD post-processing of 2.9
356 times, resulting in an endurance limit stress 2.9 times greater than in the as-built condition according to Equation 1.

357 Table 5. Surface roughness parameters and stress concentration factor determined with Equation 2

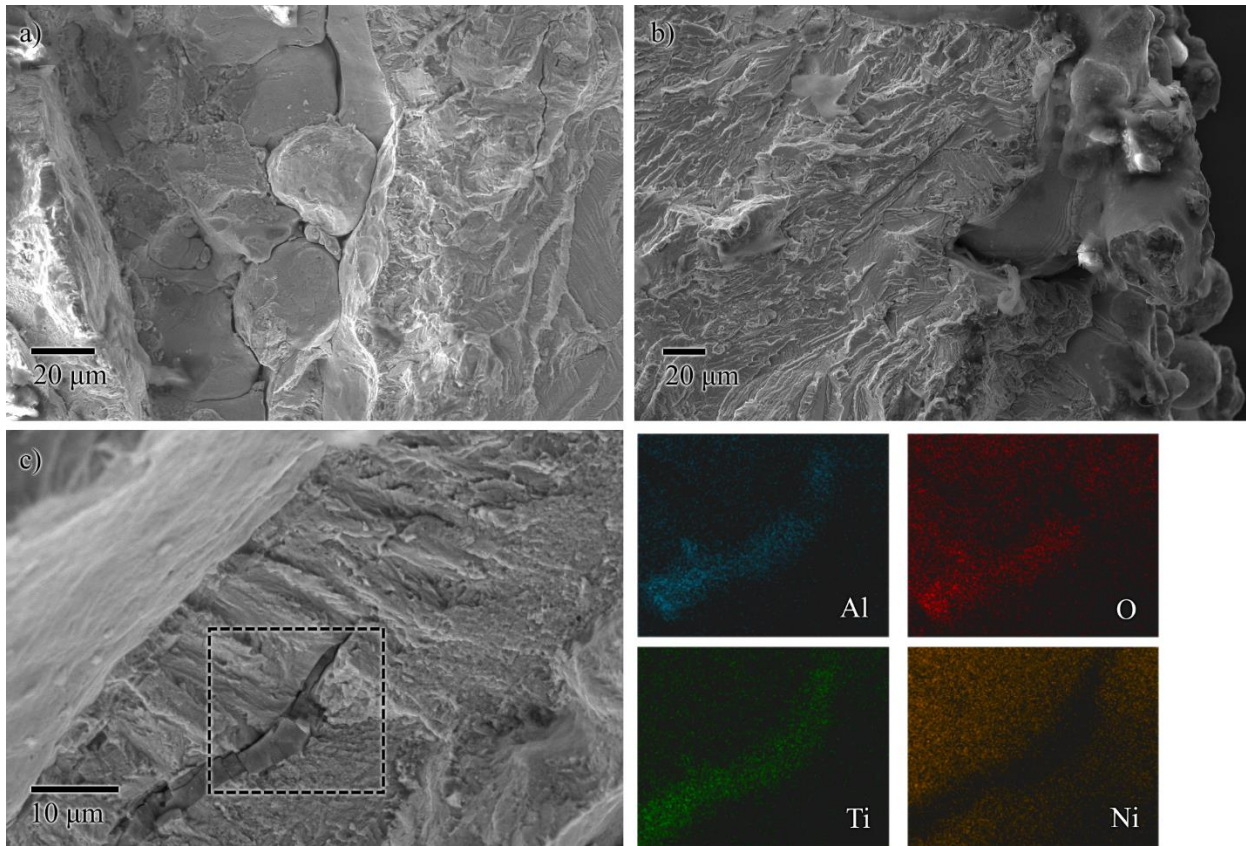|	As-built	ESD + HP
S_a [μm]	13.2	2.4
S_y [μm]	152.48	90.54
S_z [μm]	73.81	34.97
ρ [μm]	8.98	8.63
K_t	7.07	2.44

358

359 Since a combination of ESD and hammer peening demonstrated a lower surface roughness than hammer peening
360 alone, a greater fatigue life for ESD+HP samples when compared to HP samples is justified. This also suggests that
361 the compressive residual stresses introduced by the peening process, which have been shown to delay crack
362 initiation and propagation originating at the surface [57], is not likely a major contributor to the improved fatigue
363 life. The presence of an ESD processed Inconel 718 coating in the ESD+HP samples is expected to account for some
364 of the difference in performance. One contributor to the improved fatigue life may be attributed to the introduction
365 of residual stresses from the quenching of deposited material during ESD. Additionally, the influence of Inconel 718's
366 better mechanical properties would be reflected in the value of ΔK_{th} in Equation 1, since the threshold stress
367 intensity factor for propagation varies depending on the material and microstructure. One benefit to ESD processed
368 Inconel 718 is the small grain size, which has been shown to improve fatigue life by increasing boundary tortuosity
369 and increasing the crack growth resistance in Ni-superalloys [58,59].

370 The lack of heat treatment in the ESD+HP condition was also found to be beneficial, since the Hastelloy X substrate
371 and Inconel 718 coating retain both their high hardness and residual stresses introduced during peening and
372 ESD/LPBF. High temperature heat treatments were found to be detrimental to fatigue life in literature, which caused
373 softening of Hastelloy X [53]. However, more modest heat treatment temperatures were also found detrimental in
374 this study. A direct aging heat treatment in ESD+HP+DA samples introduced γ″ precipitates to increase strength in
375 the Inconel 718 coating (Figure 11a), yet still resulted in a smaller fatigue life improvement over the as-built condition
376 when compared to ESD+HP samples (Figure 14). Since temperatures and heat treatment times are too low to relieve
377 residual stresses from the LPBF, ESD, or hammer peening processes (as concluded from Figure 11a), one potential
378 cause is the formation of detrimental grain boundary carbide or sigma phases in the Hastelloy X. These have been
379 found to reduce room-temperature ductility in the temperature range used for direct aging in this study [52].
380 However, these precipitates are less brittle at elevated temperatures and were found to not influence the typical
381 service temperature properties of Hastelloy X [52]. Although further studies are required to identify the influence of
382 heat treatment on the microstructure and fatigue properties of LPBF-made Hastelloy X, the decrease in fatigue
383 performance between ESD+HP and ESD+HP+DA samples indicates that the room-temperature fatigue performance
384 is highly sensitive to Hastelloy X's heat treatment response.

385 Fracture surface analysis was performed on the only ESD+HP sample that failed at an HCF stress level of 350 MPa.
386 Several sub-surface lack of fusion defects like the one shown in Figure 15a were identified near the surface of this
387 sample, with failure appearing to originate from these defects. The close proximity of these defects to the surface
388 of the part is likely responsible for the premature failure, with previous studies having shown that defects nearer
389 the surface result in a lower fatigue life [60]. An analysis of an as-built sample tested at a LCF stress level of 550 MPa

shows that failure originated from roughness-related defects on the part surface, as can be seen in Figure 15b. This also remains true of ESD+HP samples tested at 550 MPa, with Figure 15c showing that cracking originates at the part surface. This alleviated initial concerns that brittle phases in the as-deposited Inconel 718 would encourage crack initiation and propagation [61]. A previous study identified a low fracture toughness along the interdendritic regions and droplet boundaries found in ESD processed Inconel 718 subjected to tensile testing [32]. However, the brittle interdendritic Laves phase that forms in Inconel 718 does not fracture at the low stresses investigated within this study, and has instead been shown to improve fatigue strength by hindering crack propagation [62]. Another concern is the large oxide phases identified within the Inconel 718 coating (Figure 9c), which show cracking prior to fatigue testing and could be considered potential crack initiation sources. No evidence of this was observed, with none of the observed oxides in close proximity to the surface (Figure 15c) acting as crack initiation sites.

Figure 15. Fracture initiation sites in a) ESD+HP sample at 350 MPa maximum stress level, b) as-built sample at 550 MPa maximum stress level, c) ESD+HP sample at 550 MPa maximum stress level with EDX map of oxide particle

4.0 Conclusions

The surface treatment of laser powder bed fusion (LPBF) made Hastelloy X samples was performed using a combined electrospark deposition (ESD) and hammer peening technique. This post-processing method addresses the surface roughness and the surface property issues of LPBF through the deposition of an Inconel 718 coating.

- A surface roughness (R_a) reduction of 82 %, surface hardness increase of 85 %, and Inconel 718 coating of 20 μm was obtained with an ESD spark time of 25 s in a 1 cm^2 area and hammer peening. Although peening reduced surface roughness, increased the hardness of the deposited coating, and increased the size of the thermo-mechanically affected zone (TMAZ), it was not found to influence the average coating thickness.

- The use of typical Inconel 718 heat treatments had limited effect on the LPBF additive manufactured Hastelloy X substrate hardness while significantly altering the microstructure and hardness of the Inconel 718 coating. Direct aged samples showed an increase in hardness alongside a precipitation of the γ'' and γ' phases. An annealing and aging heat treatment partially recrystallized the Inconel 718 grain structure and eliminated the TMAZ prior to forming the strengthening γ'' and γ' phases.
- The use of an ESD Inconel 718 coating and hammer peening on LPBF additive manufactured Hastelloy X resulted in a greater than 50 times improvement in fatigue life (reaching $> 10^7$ cycles) at a stress of 350 MPa and an up to 5 times improvement in fatigue life (to 1.5×10^5 cycles) at a stress of 550 MPa. The improvement in the endurance limit can be primarily attributed to a reduction in surface roughness and better properties of the coating material.

Acknowledgements

References

[1] S. Afkhami, M. Dabiri, S.H. Alavi, T. Björk, A. Salminen, Fatigue characteristics of steels manufactured by selective laser melting, Int. J. Fatigue. 122 (2019) 72–83. https://doi.org/10.1016/j.ijfatigue.2018.12.029.

[2] G. Kasperovich, J. Hausmann, Improvement of fatigue resistance and ductility of TiAl6V4 processed by selective laser melting, J. Mater. Process. Technol. 220 (2015) 202–214. https://doi.org/10.1016/j.jmatprotec.2015.01.025.

[3] S. Bagehorn, J. Wehr, H.J. Maier, Application of mechanical surface finishing processes for roughness reduction and fatigue improvement of additively manufactured Ti-6Al-4V parts, Int. J. Fatigue. 102 (2017) 135–142. https://doi.org/10.1016/j.ijfatigue.2017.05.008.

[4] K. Bammert, H. Sandstede, Measurements of the Boundary Layer Development Along a Turbine Blade With Rough Surfaces., Am. Soc. Mech. Eng. 102 (1980) 978–983.

[5] Y. Il Yun, I.Y. Park, S.J. Song, Performance degradation due to blade surface roughness in a single-stage axial turbine, J. Turbomach. 127 (2005) 137–143. https://doi.org/10.1115/1.1811097.

[6] Q. Zhang, P.M. Ligrani, Aerodynamic losses of a cambered turbine vane: Influences of surface roughness and freestream turbulence intensity, J. Turbomach. 128 (2006) 536–546. https://doi.org/10.1115/1.2185125.

[7] Z. Chen, X. Wu, D. Tomus, C.H.J. Davies, Surface roughness of Selective Laser Melted Ti-6Al-4V alloy components, Addit. Manuf. 21 (2018) 91–103. https://doi.org/10.1016/j.addma.2018.02.009.

[8] U. Ali, R. Esmaeilizadeh, F. Ahmed, D. Sarker, W. Muhammad, A. Keshavarzkermani, Y. Mahmoodkhani, E. Marzbanrad, E. Toyserkani, Identification and characterization of spatter particles and their effect on surface roughness, density and mechanical response of 17-4 PH stainless steel laser powder-bed fusion parts, Mater. Sci. Eng. A. 756 (2019) 98–107. https://doi.org/10.1016/j.msea.2019.04.026.

[9] R. Esmaeilizadeh, U. Ali, A. Keshavarzkermani, Y. Mahmoodkhani, E. Marzbanrad, E. Toyserkani, On the effect of spatter particles distribution on the quality of Hastelloy X parts made by laser powder-bed fusion additive manufacturing, J. Manuf. Process. 37 (2019) 11–20. https://doi.org/10.1016/j.jmapro.2018.11.012.

[10] Z. Dong, Y. Liu, W. Li, J. Liang, Orientation dependency for microstructure, geometric accuracy and

454   mechanical properties of selective laser melting AlSi10Mg lattices, J. Alloys Compd. 791 (2019) 490–500.
455   https://doi.org/10.1016/j.jallcom.2019.03.344.

456 [11]   F. Calignano, Investigation of the accuracy and roughness in the laser powder bed fusion process, Virtual
457   Phys. Prototyp. 13 (2018) 97–104. https://doi.org/10.1080/17452759.2018.1426368.

458 [12]   T. Yang, T. Liu, W. Liao, E. MacDonald, H. Wei, X. Chen, L. Jiang, The influence of process parameters on
459   vertical surface roughness of the AlSi10Mg parts fabricated by selective laser melting, J. Mater. Process.
460   Technol. 266 (2019) 26–36. https://doi.org/10.1016/j.jmatprotec.2018.10.015.

461 [13]   R. Mertens, S. Clijsters, K. Kempen, J.-P. Kruth, Optimization of Scan Strategies in Selective Laser Melting of
462   Aluminum Parts With Downfacing Areas, J. Manuf. Sci. Eng. 136 (2014) 061012.
463   https://doi.org/10.1115/1.4028620.

464 [14]   S. Patel, A. Rogalsky, M. Vlasea, Towards understanding side-skin surface characteristics in laser powder
465   bed fusion, J. Mater. Res. (2020). https://doi.org/10.1557/jmr.2020.125.

466 [15]   O. Oyelola, P. Crawforth, R. M'Saoubi, A.T. Clare, Machining of Additively Manufactured Parts: Implications
467   for Surface Integrity, Procedia CIRP. 45 (2016) 119–122. https://doi.org/10.1016/j.procir.2016.02.066.

468 [16]   G. Rotella, S. Imbrogno, S. Candamano, D. Umbrello, Surface integrity of machined additively
469   manufactured Ti alloys, J. Mater. Process. Technol. 259 (2018) 180–185.
470   https://doi.org/10.1016/j.jmatprotec.2018.04.030.

471 [17]   I.A. Choudhury, M.A. El-Baradie, Machinability of nickel-base super alloys: A general review, J. Mater.
472   Process. Technol. 300 (1998) 278–284. https://doi.org/10.1016/s0924-0136(97)00429-9.

473 [18]   D. Loaldi, M. Kain, G. Tosello, Comparison of Selective Laser Melting Post-Processes based on Amplitude
474   and Functional Surface Roughness parameters, in: Jt. Spec. Interes. Gr. Meet. between Euspen ASPE Adv.
475   Precis. Addit. Manuf., 2019.

476 [19]   A. Lamikiz, J.A. Sánchez, L.N. López de Lacalle, J.L. Arana, Laser polishing of parts built up by selective laser
477   sintering, Int. J. Mach. Tools Manuf. 47 (2007) 2040–2050.
478   https://doi.org/10.1016/j.ijmachtools.2007.01.013.

479 [20]   K.C. Yung, T.Y. Xiao, H.S. Choy, W.J. Wang, Z.X. Cai, Laser polishing of additive manufactured CoCr alloy
480   components with complex surface geometry, J. Mater. Process. Technol. 262 (2018) 53–64.
481   https://doi.org/10.1016/j.jmatprotec.2018.06.019.

482 [21]   X. Wang, S. Li, Y. Fu, H. Gao, Finishing of additively manufactured metal parts by abrasive flow machining,
483   Solid Free. Fabr. 2016 Proc. 27th Annu. Int. Solid Free. Fabr. Symp. - An Addit. Manuf. Conf. SFF 2016.
484   (2016) 2470–2472.

485 [22]   E. Uhlmann, C. Schmiedel, J. Wendler, CFD simulation of the Abrasive Flow Machining process, Procedia
486   CIRP. 31 (2015) 209–214. https://doi.org/10.1016/j.procir.2015.03.091.

487 [23]   S. Sarkar, C.S. Kumar, A.K. Nath, Effects of different surface modifications on the fatigue life of selective
488   laser melted 15–5 PH stainless steel, Mater. Sci. Eng. A. 762 (2019) 138109.
489   https://doi.org/10.1016/j.msea.2019.138109.

490 [24]   V. Urlea, V. Brailovski, Electropolishing and electropolishing-related allowances for powder bed selectively
491   laser-melted Ti-6Al-4V alloy components, J. Mater. Process. Technol. 242 (2017) 1–11.
492   https://doi.org/10.1016/j.jmatprotec.2016.11.014.

493 [25]   D. Zhu, L. Yu, R. Zhang, Dissolution effects with different microstructures of inconel 718 on surface integrity
494   in electrochemical machining, J. Electrochem. Soc. 165 (2018) E872–E878.
495   https://doi.org/10.1149/2.0761816jes.

496 [26]   E.J. Taylor, M. Inman, Electrochemical surface finishing, Electrochem. Soc. Interface. 23 (2014) 57–61.
497   https://doi.org/10.1149/2.F05143if.

498 [27]   V. Finazzi, A.G. Demir, C.A. Biffi, F. Migliavacca, L. Petrini, B. Previtali, Design and functional testing of a
499   novel balloon-expandable cardiovascular stent in CoCr alloy produced by selective laser melting, J. Manuf.

500   Process. 55 (2020) 161–173. https://doi.org/10.1016/j.jmapro.2020.03.060.

501   [28]   M. Anilli, A.G. Demir, B. Previtali, Additive manufacturing of laser cutting nozzles by SLM: processing,
502   finishing and functional characterization, Rapid Prototyp. J. 24 (2018) 562–583.
503   https://doi.org/10.1108/RPJ-05-2017-0106.

504   [29]   A. Cutolo, B. Neirinck, K. Lietaert, C. de Formanoir, B. Van Hooreweder, Influence of layer thickness and
505   post-process treatments on the fatigue properties of CoCr scaffolds produced by laser powder bed fusion,
506   Addit. Manuf. 23 (2018) 498–504. https://doi.org/10.1016/j.addma.2018.07.008.

507   [30]   L. Denti, A. Sola, On the Effectiveness of Different Surface Finishing Techniques on A357.0 Parts Produced
508   by Laser-Based Powder Bed Fusion: Surface Roughness and Fatigue Strength, Metals (Basel). 9 (2019) 1284.
509   https://doi.org/10.3390/met9121284.

510   [31]   M.J. Donachie, S.J. Donachie, Superalloys: A Technical Guide, ASM International, 2002.
511   https://doi.org/10.1361/stgs2002p001.

512   [32]   P.D. Enrique, Z. Jiao, N.Y. Zhou, E. Toyserkani, Effect of microstructure on tensile properties of electrospark
513   deposition repaired Ni-superalloy, Mater. Sci. Eng. A. 729 (2018) 268–275.
514   https://doi.org/10.1016/j.msea.2018.05.049.

515   [33]   P.D. Enrique, Z. Jiao, N.Y. Zhou, Effect of Direct Aging on Heat-Affected Zone and Tensile Properties of
516   Electrospark-Deposited Alloy 718, Metall. Mater. Trans. A. 50 (2019) 285–294.
517   https://doi.org/10.1007/s11661-018-4997-1.

518   [34]   J.R. Davis, ASM Specialty Handbook: Heat-Resistant Materials, ASM International, 1997.

519   [35]   S. Sui, C. Zhong, J. Chen, A. Gasser, W. Huang, J.H. Schleifenbaum, Influence of solution heat treatment on
520   microstructure and tensile properties of Inconel 718 formed by high-deposition-rate laser metal
521   deposition, J. Alloys Compd. 740 (2018) 389–399. https://doi.org/10.1016/j.jallcom.2017.11.004.

522   [36]   J. Vit, Surface metrology open profile Gaussian filter, (2015).
523   https://www.mathworks.com/matlabcentral/fileexchange/52892-surface-metrology-open-profile-
524   gaussian-filter.

525   [37]   S. Frangini, A. Masci, A study on the effect of a dynamic contact force control for improving electrospark
526   coating properties, Surf. Coatings Technol. 204 (2010) 2613–2623.
527   https://doi.org/10.1016/j.surfcoat.2010.02.006.

528   [38]   A. V. Ribalko, K. Korkmaz, O. Sahin, Intensification of the anodic erosion in electrospark alloying by the
529   employment of pulse group, Surf. Coatings Technol. 202 (2008) 3591–3599.
530   https://doi.org/10.1016/j.surfcoat.2007.12.037.

531   [39]   K.F. Weaver, V.C. Morales, S.L. Dunn, K. Godde, P.F. Weaver, An Introduction to Statistical Analysis in
532   Research: With Applications in the Biological and Life Sciences, 2017.
533   https://doi.org/10.1002/9781119454205.

534   [40]   E. Hosseini, V.A. Popovich, A review of mechanical properties of additively manufactured Inconel 718,
535   Addit. Manuf. 30 (2019) 100877. https://doi.org/10.1016/j.addma.2019.100877.

536   [41]   E. Anisimov, A.K. Khan, O.A. Ojo, Analysis of microstructure in electro-spark deposited IN718 superalloy,
537   Mater. Charact. 119 (2016) 233–240. https://doi.org/10.1016/j.matchar.2016.07.025.

538   [42]   P.D. Enrique, Z. Jiao, N.Y. Zhou, E. Toyserkani, Dendritic coarsening model for rapid solidification of Ni-
539   superalloy via electrospark deposition, J. Mater. Process. Technol. 258 (2018) 138–143.
540   https://doi.org/10.1016/j.jmatprotec.2018.03.023.

541   [43]   T.B. Reed, Free Energy of Formation of Binary Compounds: An Atlas of Charts for High-temperature
542   Chemical Calculations, MIT Press, 1971.

543   [44]   A.N.D. Gasper, B. Szost, X. Wang, D. Johns, S. Sharma, A.T. Clare, I.A. Ashcroft, Spatter and oxide formation
544   in laser powder bed fusion of Inconel 718, Addit. Manuf. 24 (2018) 446–456.
545   https://doi.org/10.1016/j.addma.2018.09.032.

546   [45]   Y.N. Zhang, X. Cao, P. Wanjara, M. Medraj, Oxide films in laser additive manufactured Inconel 718, Acta
547   Mater. 61 (2013) 6562–6576. https://doi.org/10.1016/j.actamat.2013.07.039.
548   [46]   L.M. Felix, C.C.F. Kwan, N.Y. Zhou, The Effect of Pulse Energy on the Defects and Microstructure of Electro-
549   Spark-Deposited Inconel 718, Metall. Mater. Trans. A. 50 (2019) 4223–4231.
550   https://doi.org/10.1007/s11661-019-05332-8.
551   [47]   S. Singh, Y. Guo, B. Winiarski, T.L. Burnett, P.J. Withers, M. De Graef, High resolution low kV EBSD of heavily
552   deformed and nanocrystalline Aluminium by dictionary-based indexing, Sci. Rep. 8 (2018) 1–8.
553   https://doi.org/10.1038/s41598-018-29315-8.
554   [48]   S. Kuroda, T.W. Clyne, The quenching stress in thermally sprayed coatings, Thin Solid Films. 200 (1991) 49–
555   66. https://doi.org/10.1016/0040-6090(91)90029-W.
556   [49]   A.J. Wilkinson, D.J. Dingley, Quantitative deformation studies using electron back scatter patterns, Acta
557   Metall. Mater. 39 (1991) 3047–3055. https://doi.org/10.1016/0956-7151(91)90037-2.
558   [50]   A. Oradei-Basile, J.F. Radavich, A Current T-T-T Diagram for Wrought Alloy 718, in: Superalloys 718, 625
559   Var. Deriv., TMS, 1991: pp. 325–335. https://doi.org/10.7449/1991/Superalloys_1991_325_335.
560   [51]   J.-C. Zhao, M. Larsen, V. Ravikumar, Phase precipitation and time–temperature-transformation diagram of
561   Hastelloy X, Mater. Sci. Eng. A. 293 (2000) 112–119. https://doi.org/10.1016/S0921-5093(00)01049-2.
562   [52]   H.M. Tawancy, Long-term ageing characteristics of Hastelloy alloy X, J. Mater. Sci. 18 (1983) 2976–2986.
563   https://doi.org/10.1007/BF00700780.
564   [53]   Q. Han, R. Mertens, M.L. Montero-Sistiaga, S. Yang, R. Setchi, K. Vanmeensel, B. Van Hooreweder, S.L.
565   Evans, H. Fan, Laser powder bed fusion of Hastelloy X: Effects of hot isostatic pressing and the hot cracking
566   mechanism, Mater. Sci. Eng. A. 732 (2018) 228–239. https://doi.org/10.1016/j.msea.2018.07.008.
567   [54]   M. Suraratchai, J. Limido, C. Mabru, R. Chieragatti, Modelling the influence of machined surface roughness
568   on the fatigue life of aluminium alloy, Int. J. Fatigue. 30 (2008) 2119–2126.
569   https://doi.org/10.1016/j.ijfatigue.2008.06.003.
570   [55]   D. Arola, C.L. Williams, Estimating the fatigue stress concentration factor of machined surfaces, Int. J.
571   Fatigue. 24 (2002) 923–930. https://doi.org/10.1016/S0142-1123(02)00012-9.
572   [56]   J.W. Pegues, N. Shamsaei, M.D. Roach, R.S. Williamson, Fatigue life estimation of additive manufactured
573   parts in the as-built surface condition, Mater. Des. Process. Commun. 1 (2019) e36.
574   https://doi.org/10.1002/mdp2.36.
575   [57]   M.A.S. Torres, H.J.C. Voorwald, An evaluation of shot peening, residual stress and stress relaxation on the
576   fatigue life of AISI 4340 steel, Int. J. Fatigue. 24 (2002) 877–886. https://doi.org/10.1016/S0142-
577   1123(01)00205-5.
578   [58]   D. Gopikrishna, S.N. Jha, L.N. Dash, Influence of Microstructure on Fatigue Properties of Alloy 718, in:
579   Superalloys 718, 625, 706 Var. Deriv., TMS, Pittsburgh, Pennsylvania, 1997: pp. 567–573.
580   https://doi.org/10.7449/1997/Superalloys_1997_567_573.
581   [59]   A.D. Boyd-Lee, Fatigue crack growth resistant microstructures in polycrystalline Ni-base superalloys for
582   aeroengines, Int. J. Fatigue. 21 (1999) 393–405. https://doi.org/10.1016/S0142-1123(98)00087-5.
583   [60]   S. Leuders, M. Thöne, A. Riemer, T. Niendorf, T. Tröster, H.A. Richard, H.J. Maier, On the mechanical
584   behaviour of titanium alloy TiAl6V4 manufactured by selective laser melting: Fatigue resistance and crack
585   growth performance, Int. J. Fatigue. 48 (2013) 300–307. https://doi.org/10.1016/j.ijfatigue.2012.11.011.
586   [61]   J.J. Schirra, R.H. Caless, R.W. Hatala, The Effect of Laves Phase on the Mechanical Properties of Wrought
587   and Cast + HIP Inconel 718, in: Superalloys 718, 625 Var. Deriv., TMS, 1991: pp. 375–388.
588   https://doi.org/10.7449/1991/Superalloys_1991_375_388.
589   [62]   S. Sui, J. Chen, E. Fan, H. Yang, X. Lin, W. Huang, The influence of Laves phases on the high-cycle fatigue
590   behavior of laser additive manufactured Inconel 718, Mater. Sci. Eng. A. 695 (2017) 6–13.
591   https://doi.org/10.1016/j.msea.2017.03.098.